

Cite this: *Dalton Trans.*, 2024, **53**,
2949

Achieving excellent energy storage performance with thermal stability in lead-free AgNbO_3 ceramics†

Wenna Chao,^{a,b} Juan Du,^a Peng Li,^a Wei Li^a and Tongqing Yang^{*b}

Large hysteresis and low energy density of pure AgNbO_3 ceramics limit their further application in pulsed power techniques. Here, less-harmful Sm_2O_3 -modified AgNbO_3 antiferroelectric ceramics were synthesized by a rolling process, in order to improve the energy storage performance. All the Sm_2O_3 -doped samples display reduced hysteresis due to disrupted long-range order, as certified by Raman spectra. As expected, due to the large dielectric breakdown strength and reduced hysteresis, an improved energy storage density, W_{rec} , of 5.85 J cm^{-3} and satisfactory energy efficiency, η , of 77% can be simultaneously achieved in the studied antiferroelectric ceramics, showing great superiority over other bulk electronic ceramics. Along with excellent temperature stability within the range of $20\text{--}150 \text{ }^\circ\text{C}$ at 320 kV cm^{-1} ($W_{\text{rec}} > 4.3 \text{ J cm}^{-3}$, with minimal variation of $\leq 4\%$) in the studied samples, this shows that AgNbO_3 -based environmentally friendly ceramics are promising materials for pulsed power techniques.

Received 24th September 2023,

Accepted 5th January 2024

DOI: 10.1039/d3dt03139j

rsc.li/dalton

1. Introduction

Niobate materials have important applications in microwave dielectric ceramics, photocatalysis, and luminescent materials, showing broad application prospects.^{1–5} However, the harsh reaction conditions and expensive raw materials required limit their further development and application.⁶ Benefiting from progress in preparation technologies, the synthesis ceramics of satisfactory quality can be realized. With the development of pulsed power technologies and the urgent need for high pulse power generators, high energy storage density, large discharge current and fast discharging speed have become research hotspots.^{7,8} Antiferroelectric materials have received renewed attention due to their unique AFE (antiferroelectric)–FE (ferroelectric) phase transition under an external electric field, and outstanding energy storage performance (rapid discharge speed, superior power density, and long cycle life). PZ(PbZrO_3) lead-based antiferroelectric materials have experienced mature development and a huge energy density of 10.4 J cm^{-3} and 12.8 J cm^{-3} have been achieved in ($\text{Pb}_{0.98}\text{La}_{0.02}$)($\text{Zr}_{0.55}\text{Sn}_{0.45}$) $_{0.995}\text{O}_3$ ⁹ and Ba-modified ($\text{Pb}_{0.95}\text{Ba}_{0.02}\text{La}_{0.02}$)

($\text{Zr}_{0.6}\text{Sn}_{0.4}$) O_3 ceramics,¹⁰ respectively. For the sake of environmental protection, lead-free antiferroelectric materials, such as AgNbO_3 ¹¹ and NaNbO_3 ,¹² are widely studied.

The double hysteresis loop of AgNbO_3 ceramics was first observed by Fu *et al.*¹¹ with a high polarization of $52 \mu\text{C cm}^{-2}$ and low efficiency of 40% at an electric field of 220 kV cm^{-1} , limiting its further application in the energy storage field. AgNbO_3 has a typical perovskite structure, which belongs to the *Pbcm* space group at room temperature.¹³ Similar to antiferroelectric NaNbO_3 ceramics, AgNbO_3 also experiences a series of phase transitions of $\text{M}_1\text{--M}_2\text{--M}_3\text{--O--T}$.^{13–15} Due to its high flexibility for adjustment of its composition and properties, much effort has been made to improve its energy storage performance. However, the low energy efficiency caused by the appearance of significant double hysteresis loops is not conducive to improvement in the energy density. Thus, La^{3+} was introduced to enhance the antiferroelectric stability, and an improved efficiency of 70% with an energy storage density, W_{rec} , of 4.4 J cm^{-3} was achieved simultaneously in ($\text{La}_{0.02}\text{Ag}_{0.94}$) NbO_3 ceramics.¹⁶ Another strategy is to introduce ions with low polarizability, such as Ta^{5+} at the B site, to increase the phase transition field, and a better energy density of 4.2 J cm^{-3} has been achieved in $\text{AgNb}_{0.85}\text{Ta}_{0.15}\text{O}_3$ ceramics.¹⁷ Luo *et al.* have successfully constructed a binary solid solution of $\text{AgNbO}_3\text{--AgTaO}_3$ ceramics, with a high W_{rec} of 6.3 J cm^{-3} and efficiency of 90%.¹⁸

Silver niobate is likely to decompose at high temperature, so it needs to be prepared in an environment with sufficient oxygen, which can only be sintered in a closed-tube furnace by the standard solid-state reaction method. Thus, the microstructure cannot be improved through the sintering process,

^aCollege of Materials Science and Engineering, Liaocheng University, Liaocheng 252059, China

^bKey Laboratory of Advanced Civil Engineering Materials of the Ministry of Education, Functional Materials Research Laboratory, School of Materials Science and Engineering, Tongji University, 4800 Cao'an Road, Shanghai 201804, China. E-mail: yangtongqing@tongji.edu.cn

† Electronic supplementary information (ESI) available. See DOI: <https://doi.org/10.1039/d3dt03139j>

and the addition property appears to be particularly critical for the enhancement of dielectric properties. Therefore, the anti-ferroelectricity can be optimized by doping modifications and thus reducing the tolerance factor of the ceramics. For the materials mentioned above, the underlying mechanisms for improving energy density are generally similar. Lanthanide-modified AN ceramics and transition metal oxides with smaller tolerance factors, such as MnO_2 , all aim to improve the breakdown field strength of the ceramic, stabilize the anti-ferroelectric phase, or improve the sintering process, to achieve the goal of increasing the energy storage density.^{19,20}

It has been reported that the addition of Sm_2O_3 is beneficial for improving the physical properties in $(\text{Bi}_{0.5}\text{Na}_{0.5})_{0.94}\text{Ba}_{0.06}\text{TiO}_3$ ceramics, which are characterized by diffuse phase transitions and relaxor behavior.^{21,22} As a high-melting component, the addition of Sm_2O_3 into AgNbO_3 ceramics will hinder grain growth, which contributes to improvement in the dielectric breakdown strength. In addition, the smaller ionic radius of Sm^{3+} (1.08 Å) compared to that of Ag^+ (1.28 Å),²³ leads to reduction of the tolerance factor, and thus is advantageous for enhancement of antiferroelectricity. Therefore, in this work, the energy storage properties of Sm_2O_3 -modified AgNbO_3 ceramics were systematically investigated. An improved energy storage density of 5.8 J cm^{-3} and high efficiency of 77% was achieved in $\text{Sm}_{0.06}\text{Ag}_{0.82}\text{NbO}_3$ lead-free ceramics with a breakdown strength (BDS) of 370 kV cm^{-1} .

2. Materials and methods

$\text{Sm}_x\text{Ag}_{1-3x}\text{NbO}_3$ ($x = 0, 0.05, 0.06, 0.07, 0.08$, abbreviated as SAN0–4) lead-free ceramics were synthesized by a rolling process. Reagent-grade oxides, Ag_2O (99.7%, Aladdin reagent), Nb_2O_5 (99.99%, Sinopharm Chemical Reagent), Sm_2O_3 (99.9%, Aladdin reagent), served as the starting materials. The starting powders were weighed according to their stoichiometric compositions and mixed thoroughly in ethanol using zirconia balls for 24 h. The dried powder was then calcined at $880 \text{ }^\circ\text{C}$ for 6 h and then ball-milled again for 24 h. Then, the pre-sintered powder was blended with 25% PVA (polyvinyl alcohol) to form ceramic tapes *via* a rolling process, with a thickness of 0.3 mm. After burning out the binder at $600 \text{ }^\circ\text{C}$ for 5 h, the sintering process was carried out on the tapes over the temperature range $1050\text{--}1080 \text{ }^\circ\text{C}$ for 6 h in a flowing O_2 atmosphere to prohibit the decomposition of Ag_2O . Silver electrodes were fired on both sides of the samples at $800 \text{ }^\circ\text{C}$ for 0.5 h.

The phase structure of the SAN x ceramics was determined by X-ray diffraction (XRD, D8 Advance; Bruker AXS GmbH, Karlsruhe, Germany), while the grain morphology of the ceramics was analyzed by field-emission scanning electron microscopy (SEM, Nova Nano SEM 450, FEI, Eindhoven, The Netherlands). Raman spectra were recorded for all samples using a Horiba Lab-Ram iHR550 spectrometer with an excitation source of 532 nm. Dielectric properties and impedance spectra were measured with a computer-controlled LCR meter (HP 4284; Hewlett Packard Co, USA), and the energy storage performance was investigated by P –

E hysteresis loops using a precision ferroelectric analyzer (Premier II, Radiant Technologies Inc., USA) equipped with a high voltage power supply (TRek Model 663A). For the P – E measurements, the samples were polished down to 0.1 mm and both sides were coated with gold electrodes of 2 mm diameter. For the charge–discharge measurements, the samples were polished down to 0.13 mm and both sides were sputtered with gold electrodes of 2 mm diameter. The samples were evaluated based on the field-dependent unipolar P – E loops.

3. Results and discussion

The permittivity of the prepared ceramics as a function of temperature is illustrated in Fig. 1a. The corresponding P – E hysteresis loops are depicted in Fig. 1b. (The full hysteresis loops are summarized in Fig. S1.†) The pure AN ceramic shows three obvious abnormal dielectric peaks, which correspond to the phase transitions of M_1 – M_2 , M_2 – M_3 , and M_3 – O , respectively. With increase in the Sm^{3+} content, all phase transition temperatures show a downward trend, coupled with a sharp drop in the permittivity. In particular, for the composition $x = 0.08$, all the dielectric peaks disappear, which reflect that the composition SAN4 has become a paraelectric phase. The phase diagram is summarized in Fig. S2.† Due to the disturbed long-range order, the antiferroelectricity was suppressed, leading to broadening of the abnormal dielectric peaks. This can also be proved by the corresponding P – E loops in Fig. 1b. The P – E loop of pure AgNbO_3 exhibits a square shape, which was characterized by high saturation and remanent polarization, low BDS, and large hysteresis (ΔE). The shape of the hysteresis loops changes from square to slanted, coupled with a reduction of the saturation polarization and hysteresis. For the composition $x = 0.08$, the hysteresis loops displayed similar behavior compared to that of linear dielectric materials with high BDS and low saturation polarization. The recoverable energy densities (W_{rec}) of the SAN0–4 ceramics are 1.49 J cm^{-3} , 4.74 J cm^{-3} , 5.85 J cm^{-3} , 3.72 J cm^{-3} , and 3.89 J cm^{-3} , respectively. The corresponding energy storage efficiencies of SAN0–4 are 25%, 73%, 77%, 72%, and 92%, respectively. The phase transition electric field (E_{F} , the AFE–FE switching electric field) was increased from 140 kV cm^{-1} for $x = 0$ to 300 kV cm^{-1} for $x = 0.07$, which also proved the enhanced stability of the antiferroelectricity. Moreover, it can be inferred that high BDS can be obtained at the sacrifice of high polarization. The corresponding BDS increased from 200 kV cm^{-1} to 400 kV cm^{-1} , which contributes to the high W_{rec} of the SAN2 ceramics. According to the definition of the tolerance factor:²⁴

$$t = \frac{R_{\text{A}} + R_{\text{O}}}{\sqrt{2}(R_{\text{B}} + R_{\text{O}})},$$

where R_{A} , R_{B} , and R_{O} represent the cation radius of the A site, B site, and O^{2-} , the reduced t indicates the enhanced antiferroelectricity. With increasing Sm^{3+} content, the value of t decreased from 0.927 for AN to 0.851 for $x = 0.08$, which also proved the enhanced antiferroelectricity.

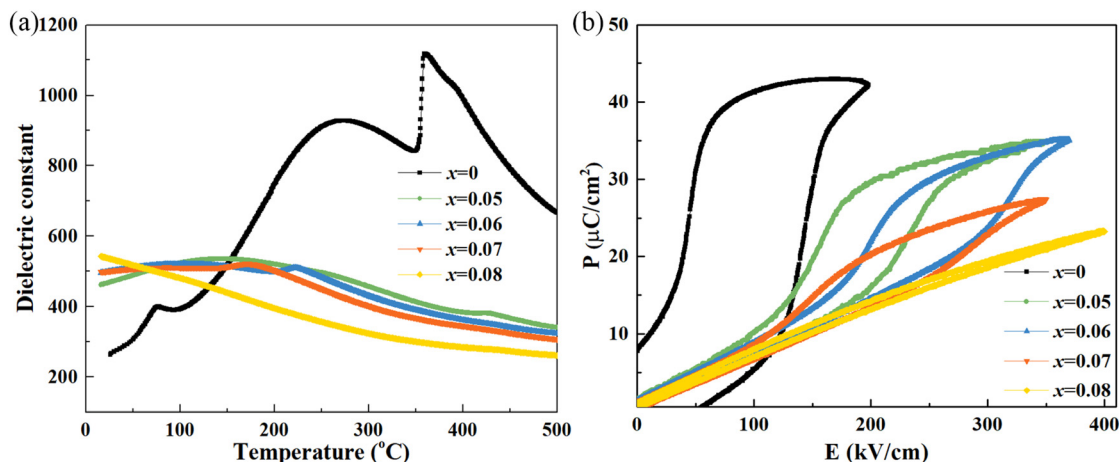


Fig. 1 (a) The temperature dependence of permittivity of the prepared ceramics measured at 100 kHz. (b) P - E loops at 10 Hz at room temperature.

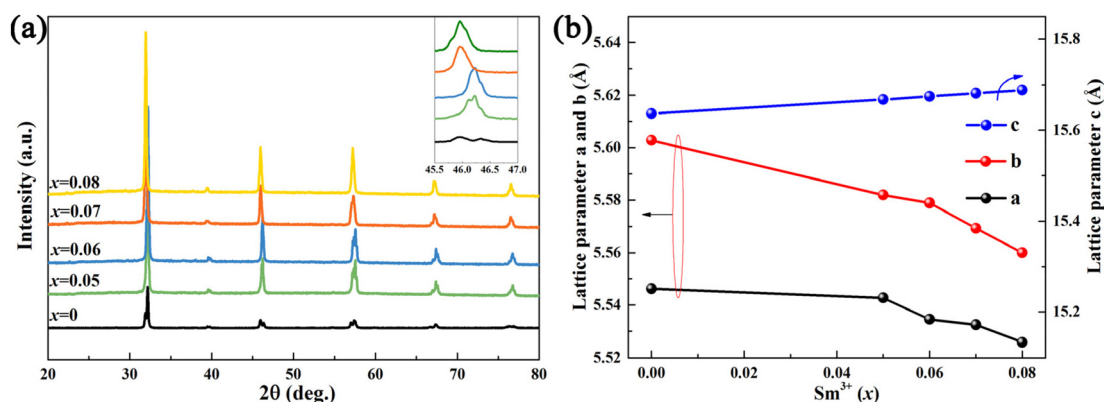


Fig. 2 (a) XRD patterns of the SAN x ceramics. (b) The lattice parameters as a function of Sm^{3+} content based on Rietveld refinement.

Fig. 2 displays the XRD patterns of the SAN x ceramics. It can be noted that all studied ceramics exhibit single perovskite structures without impurity or a second phase. With increasing Sm^{3+} content, from 0 to 0.08, the split peaks around 45° have disappeared and present a pseudo cubic phase, which is consistent with the results in Fig. 1a, indicating that the phase of the SAN x ceramic has changed into a paraelectric state at room temperature. The obtained lattice parameters (a , b , and c) based on Rietveld refinement are depicted in Fig. 2b. More details can be found in Fig. S3 (ESI †). The lower fitting values of R_{wp} and R_{p} indicate that the structural model used for the structure refinement is reliable. We note that a and b show a decreasing trend, while c increases with increasing Sm^{3+} content, thus leading to cell volume shrinkage. Because the radius of Sm^{3+} (1.08 \AA) is very similar to that of Ag^+ (1.28 \AA), it is possible that Sm^{3+} prefers to occupy the A site and affects the properties of the AN ceramics.²³ With higher Sm^{3+} content, the cell volume decreased from 485.9 \AA^3 to 482 \AA^3 (Fig. S3f, ESI †), indicating that Sm^{3+} has successfully incorporated into the AgNbO_3 lattice.

The surface morphologies of the SAN x ceramics are presented in Fig. 3. It can be seen that the pure AgNbO_3 ceramic possesses a loose structure with visible pores and an inhomogeneous

distribution. Compared with pure AgNbO_3 ceramic, the composition of the Sm^{3+} -doped ceramics show a denser microstructure. In general, the relationship between average grain size (AG) and dielectric breakdown field (BDS) is as follows:²⁵

$$\text{BDS} \propto \frac{1}{\sqrt{\text{AG}}} \quad (1)$$

From this equation we can see that the breakdown field strength of the ceramics can be improved by refining the grain size under the condition where the ceramics are kept compact. The BDS was evaluated using the Weibull distribution, as shown in Fig. 3f, which was calculated by the following equation:²⁶

$$X_i = \ln E_i \quad (2)$$

$$Y_i = \ln \left(-\ln \left(1 - \frac{i}{n+1} \right) \right) \quad (3)$$

where E is the BDS of each specimen and n is the total sum of samples, respectively. As expected, the AG decreased, from 2.96 \mu m for $x = 0$ to 1.49 \mu m for $x = 0.08$, due to the high

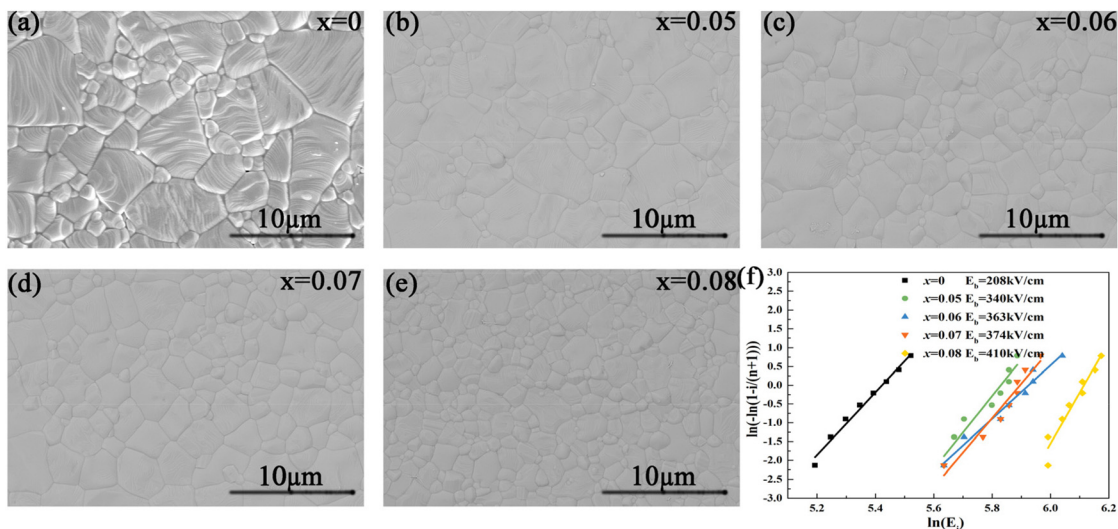


Fig. 3 (a)–(e) The surface microstructure images and (f) Weibull distribution of SAN0–4 ceramics.

melting point component the added Sm_2O_3 , resulting in the BDS increasing from 208 kV cm^{-1} to 410 kV cm^{-1} , as shown in Fig. 3f. This indicates that smaller grain size and higher compactness are indeed beneficial to improving the dielectric breakdown strength of the SANx ceramics.

The intensity and position of the Raman peaks are closely related to the crystal structure, so the change in the microstructure can be reflected by the Raman vibration modes.^{27,28} Raman spectra were measured to further investigate the local structure evolution of the SANx ceramics. It can be seen that pure AgNbO_3 ceramic shows intense internal vibration modes (ν_1, ν_2), bending vibration modes (ν_3, ν_4) of BO_6 octahedral tilting, and stretching vibration modes (ν_5, ν_6), which are typical features of the M_1 phase structure at room temperature.⁵ Of particular importance is that, with increase in Sm^{3+} content, all the Raman peaks become broad and diffuse, which can be ascribed to the increased disorder of the local

structure induced by the free occupation and disordered arrangement of Sm^{3+} at the A site, that is, the relaxation of the ceramics is enhanced.^{27,29} Another reason is that the chemical heterogeneity leads to peak broadening. With increase in Sm^{3+} content, the gradual decrease in lattice polarity also results in a gradual decline in the intensity of the Raman peaks. For the SAN4 composition, the ceramic has changed completely to a paraelectric cubic state, where the peaks exhibit a single peak. This agrees with the above results obtained by XRD and the permittivity as a function of temperature. In addition, the fluctuation of ν_3, ν_4 , and ν_6 is very sensitive to change in the phase structure of AFE ceramics, so it is usually used to judge the phase transition caused by component variation, as shown in Fig. 4b. The wavenumbers of ν_3, ν_4 , and ν_6 show a downward trend with increasing Sm^{3+} content. This is mostly because with increasing Sm^{3+} content, the disorder of the material structure gradually increases, and the polarizability of the

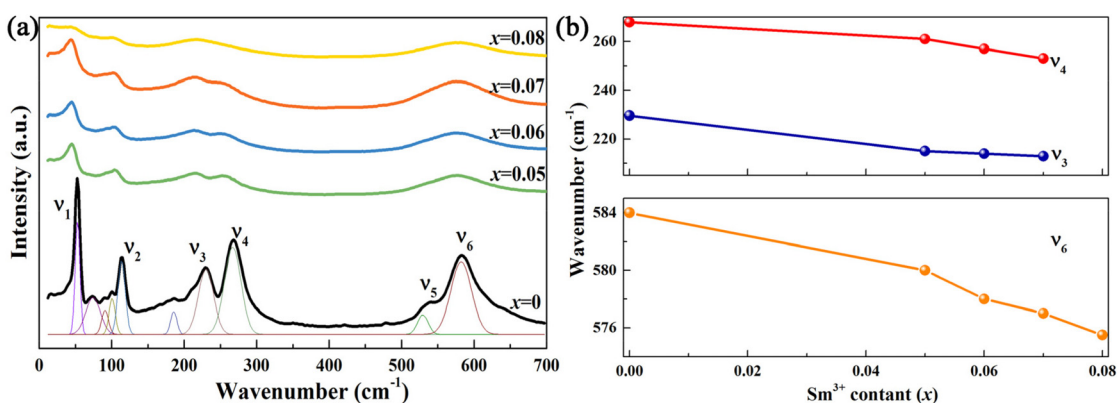


Fig. 4 (a) Raman spectra of the prepared ceramics. All the Raman spectra have been deconvoluted according to the Lorentz peak functions. (b) Evolution of the wavenumber for Raman vibration modes (ν_3, ν_4 and ν_6) for SANx ceramics.

crystal cell gradually decreases.³⁰ The ν_3 and ν_4 peaks have merged into a broad peak for $x = 0.08$, which indicates that a possible phase transition of M_3 -O has occurred.

The performance stability is an important feature for practical applications. Fig. 5a shows the P - E loops of the SAN2 ceramics from 20 to 150 °C. To avoid breakdown, the testing electric field was set at 320 kV cm⁻¹. All samples exhibited slim antiferroelectric hysteresis loops from 20 °C to 150 °C. As shown in Fig. 5a, both P_{\max} (the maximum polarization) and P_r (the remanent polarization) exhibit a tiny increasing trend (P_{\max} : from 32.08 to 33.41 $\mu\text{C cm}^{-2}$, P_r : from 4.94 to 6.52 $\mu\text{C cm}^{-2}$, summarized in Fig. S4a†), which is induced by the decreased grain size increasing the response rate of the dipole to an external electric field during the thermal activation process. The corresponding energy density W_t , W_{rec} , and the efficiency η are plotted in Fig. 5b. The value of W_{rec} decreases from 4.38 J cm⁻³ to 4.2 J cm⁻³. Fig. 5c shows the frequency stability of the SAN2 ceramics in the range 1–100 Hz at 360 kV cm⁻¹. All samples exhibit antiferroelectric loops from 1 to 100 Hz, leading to a nearly hysteresis-free polarization response at high electric field. Within the test frequency, P_{\max} reduces from 35.13 $\mu\text{C cm}^{-2}$ to 34.7 $\mu\text{C cm}^{-2}$, while P_r was found to exhibit minute changes (summarized in Fig. S4b†). As a result,

the value of W_{rec} was maintained at more than 5.5 J cm⁻³ with a high efficiency of 77%. Undoubtedly, the SAN2 ceramics exhibit excellent thermal stability with $W_{\text{rec}} > 4.2 \text{ J cm}^{-3}$ and $\eta > 65\%$ within 20–150 °C, coupled with a good frequency stability of $W_{\text{rec}} > 5.5 \text{ J cm}^{-3}$ compared to other bulk ceramics, which is particularly beneficial for energy storage technologies.

From a practical point of view, the charge-discharge performance of $(\text{Sm}_{0.06}\text{Ag}_{0.82})\text{NbO}_3$ ceramics was evaluated using an RLC (resistor, inductor, capacitor) circuit. The underdamped discharge I - t curves of the SAN2 ceramic at ambient temperature are shown in Fig. 6a. The samples exhibit discharge curves similar to sine waves under elevated electric fields. With increase in the electric field, the peak value of the first current peak also increases gradually. The current reached a maximum value of 30 A at 320 kV cm⁻¹, corresponding to the phase transition AFE-FE. Here, the corresponding discharge energy density (D_{dis}) and power density can be obtained by the following equation:³¹

$$D_{\text{dis}} = I_{\text{max}}S^{-1} \quad (4)$$

$$P_{\text{max}} = EI_{\text{max}}/2S \quad (5)$$

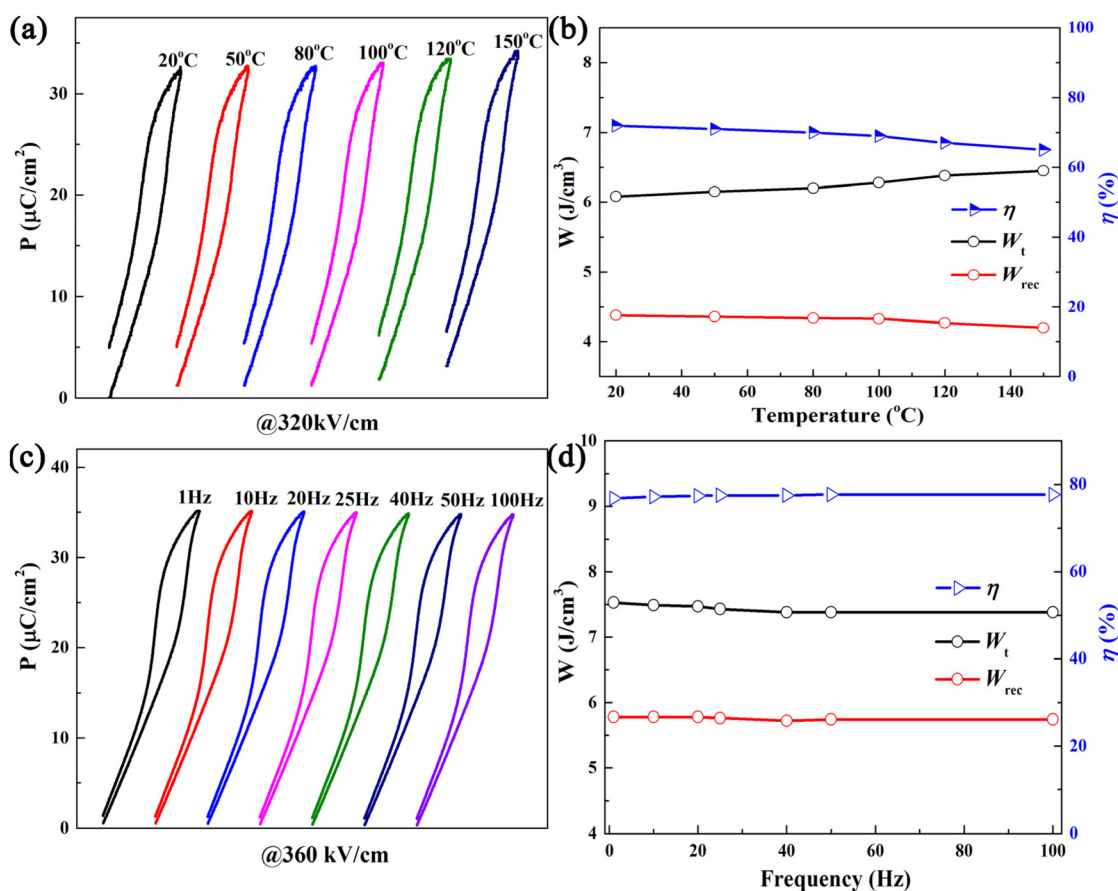


Fig. 5 (a) P - E loops of the SAN2 composition from 20 to 150 °C with 320 kV cm⁻¹ at 10 Hz. (b) Calculated W_t , W_{rec} and η from (a). (c) P - E loops of the SAN2 composition from 1 to 100 Hz with 360 kV cm⁻¹ at room temperature. (d) Calculated W_t , W_{rec} and η from (c).

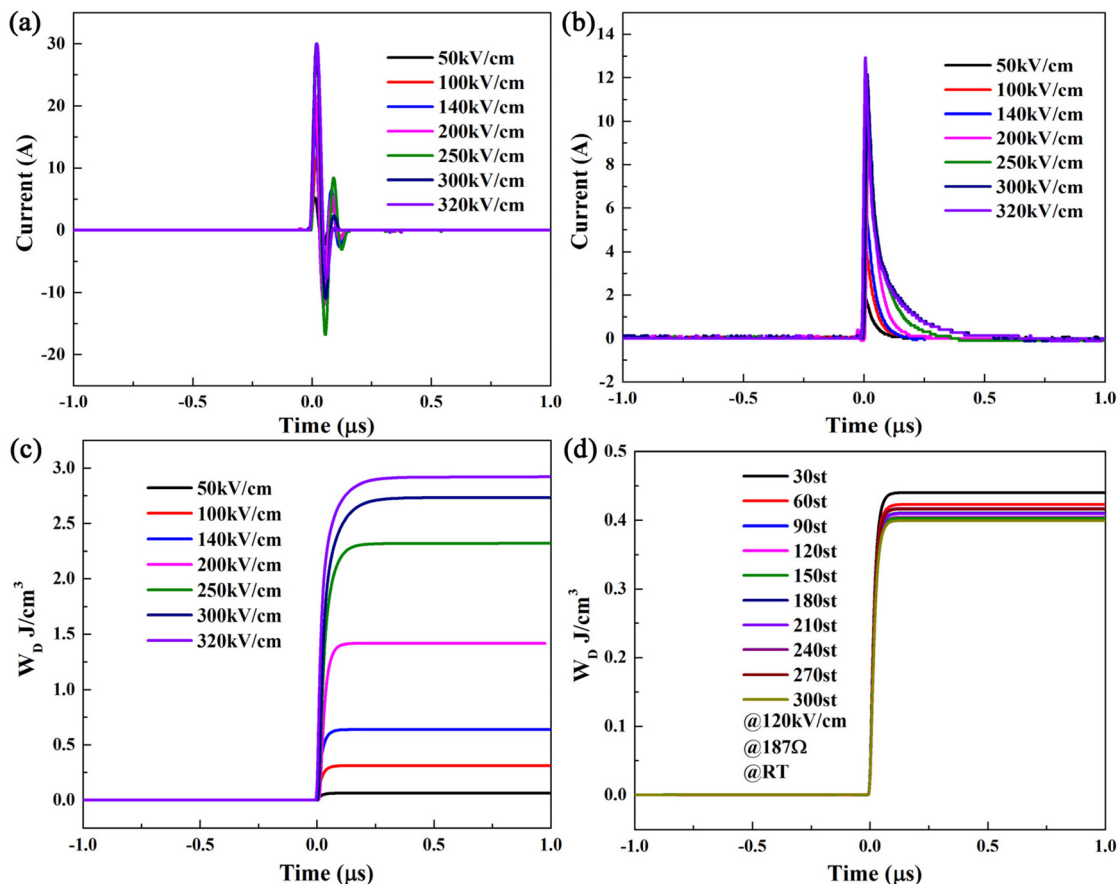


Fig. 6 (a) Underdamped discharge $I-t$ curves of SAN2 ceramics. (b) Pulsed discharge current waveforms of SAN2 ceramics curves at room temperature. (c) The relationship between W_D and discharge time at various electric fields. (d) Cyclic ability under 120 kV cm^{-1} at room temperature.

where E is external electric field and S is the electrode area, respectively. Thus, in SAN2 ceramics, the power density and discharge energy density can reach up to 955 A cm^{-2} and 153 MW cm^{-3} , respectively. Fig. 6b illustrates the pulsed discharge $I-t$ curves at elevated electric fields. The peak current values increased from 1.82 A at 50 kV cm^{-1} to 12.95 A at 320 kV cm^{-1} . Based on the results in Fig. 6b, the discharge energy density W_D can be acquired by the following equation:³¹

$$W_D = R \int i(t)^2 dt / V \quad (6)$$

where $i(t)$, R , and V are the discharging current curves, the total load resistance, and the sum of the volume, respectively. Fig. 6c shows the corresponding calculated W_D-t curves. The value of W_D rises gradually from 0.06 J cm^{-3} at 50 kV cm^{-1} to 2.92 J cm^{-3} at 320 kV cm^{-1} . Furthermore, the definition of $t_{0.9}$ can be expressed as the time required to release 90% of the energy, which is widely used to assess the discharge speed of ceramics. In this work, a rapid discharge speed ($t_{0.9} = 88 \text{ ns}$) was observed in SAN2 ceramics at 320 kV cm^{-1} . Fig. 6d shows the cyclic stability the SAN2 ceramics at 120 kV cm^{-1} . The W_D values display a fluctuating change ($0.44-0.4 \text{ J cm}^{-3}$, with minimal variation $<9\%$) over a cycle range of 1–300. This

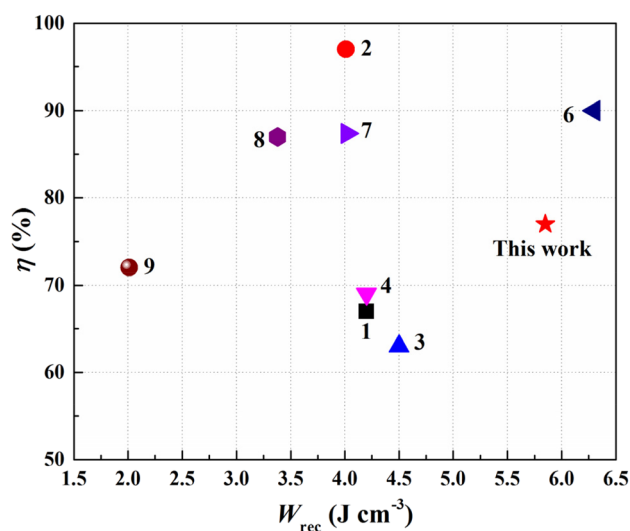


Fig. 7 Comparison of W_{rec} and efficiency in bulk ceramics reported in previous works. (1 is BNBT-CH;³² 2 is 0.9KNN-0.1BZN;³³ 3 is ASN;³⁴ 4 is ANT;¹⁷ 6 is AN-AT;¹⁸ 7 is 0.925KNN-0.075BZTN;³⁵ 8 is BT-BMH;³⁶ 9 is BNT-BA-xNN³⁷).

demonstrates that the studied SAN2 ceramics discharge high energy in a very short time, presenting outstanding charge–discharge capacity. This behavior reveals that these AgNbO₃-based ceramics show the advantages needed to meet the demands of pulsed power technologies.

For ease of comparison with other lead-free bulk ceramics, the energy storage density and efficiency from recently reported research are shown in Fig. 7. Among these, Ag_{0.82}Sm_{0.06}O₃ ceramics exhibit large energy density (5.85 J cm⁻³) with high energy storage efficiency (77%), showing great superiority for pulsed power capacitors.

4. Conclusions

In conclusion, Sm₂O₃-modified AgNbO₃ lead-free ceramics were synthesized by a rolling technique. Doping with Sm³⁺ is effective in hindering grain growth and enhancing the stability of the antiferroelectricity. The disrupted long-range order is beneficial to reduction in the hysteresis, which was proved by Raman spectra. Due to the large BDS and reduced hysteresis, a favorable W_{rec} of 5.85 J cm⁻³ and efficiency of 77% were achieved simultaneously in the (Sm_{0.06}Ag_{0.82})NbO₃ ceramics. For high Sm³⁺ content, the phase transition temperatures of M₁-M₂-M₃-O-T showed a downward trend and even shifted below room temperature. Therefore, an outstanding frequency stability over the range of 1–100 Hz at 360 kV cm⁻¹ ($W_{\text{rec}} > 5.5$ J cm⁻³) and thermal stability within 20–150 °C at 320 kV cm⁻¹ ($W_{\text{rec}} > 4.2$ J cm⁻³, with minimal variation of ≤4%) was observed. Furthermore, the studied ceramics also show satisfactory charge–discharge performance, with rapid discharging speed ($t_{0.9} = 88$ ns) and high discharge energy density ($W_{\text{d}} = 2.92$ J cm⁻³). The above results demonstrate that AgNbO₃-based environmentally friendly ceramics are promising materials for pulsed power techniques.

Conflicts of interest

The authors declare no conflict of interest.

Acknowledgements

This work was supported by the National Natural Science Foundation of China (No. 51872202, 51472181).

References

- H. Hughes, D. M. Iddles and I. M. Reaney, *Appl. Phys. Lett.*, 2001, **79**, 2952–2954.
- R. Yimnirun, S. Ananta and P. Laoratanakul, *J. Eur. Ceram. Soc.*, 2005, **25**, 3235–3242.
- Y. Hu and L. Guo, *ChemCatChem*, 2015, **7**, 584–587.
- Y. Su, L. Peng, C. Du and X. Wang, *J. Phys. Chem. C*, 2011, **116**, 15–21.
- H. U. Khan, K. Alam, M. Mateenullah, T. Blaschke and B. S. Haq, *J. Eur. Ceram. Soc.*, 2015, **35**, 2775–2789.
- I. Levin, J. C. Woicik, A. Llobet, M. G. Tucker, V. Krayzman, J. Pokorny and I. M. Reaney, *Chem. Mater.*, 2010, **22**, 4987–4995.
- X. Hao, J. Zhai, L. B. Kong and Z. Xu, *Prog. Mater. Sci.*, 2014, **63**, 1–57.
- Z. Liu, T. Lu, J. Ye, G. Wang, X. Dong, R. Withers and Y. Liu, *Adv. Mater. Technol.*, 2018, **3**, 1800111.
- H. Wang, Y. Liu, T. Yang and S. Zhang, *Adv. Funct. Mater.*, 2019, **29**, 1807321.
- G. Ge, K. Huang, S. Wu, F. Yan, X. Li, B. Shen and J. Zhai, *Energy Storage Mater.*, 2021, **35**, 114–121.
- D. Fu, M. Endo, H. Taniguchi, T. Taniyama and M. Itoh, *Appl. Phys. Lett.*, 2007, **90**, 252907.
- H. Qi, R. Zuo, A. Xie, A. Tian, J. Fu, Y. Zhang and S. Zhang, *Adv. Funct. Mater.*, 2019, **29**, 1903877.
- A. Kania, K. Roleder, G. E. Kugel and M. D. Fontana, *J. Phys. C: Solid State Phys.*, 1986, **19**, 9–20.
- A. Ratuszna, J. Pawluk and A. Kania, *Phase Transitions*, 2003, **76**, 611–620.
- S. Rayaprol, V. Siruguri, S. Asthana, M. K. Niranjana and K. Prasad, *J. Phys. D: Appl. Phys.*, 2015, **48**, 215303.
- J. Gao, Y. Zhang, L. Zhao, K.-Y. Lee, Q. Liu, A. Studer, M. Hinterstein, S. Zhang and J.-F. Li, *J. Mater. Chem. A*, 2019, **7**, 2225–2232.
- L. Zhao, Q. Liu, J. Gao, S. Zhang and J. F. Li, *Adv. Mater.*, 2017, **29**, 1701824.
- N. Luo, K. Han, M. J. Cabral, X. Liao, S. Zhang, C. Liao, G. Zhang, X. Chen, Q. Feng, J. F. Li and Y. Wei, *Nat. Commun.*, 2020, **11**, 4824.
- L. Zhao, Q. Liu, S. Zhang and J.-F. Li, *J. Mater. Chem. C*, 2016, **4**, 8380–8384.
- Z. Xu, Y. Feng, S. Zheng, A. Jin, F. Wang and X. Yao, *Mater. Sci. Eng., B*, 2003, **99**, 441–444.
- F. Xue, L. Liang, Y. Gu, I. Takeuchi, S. V. Kalinin and L.-Q. Chen, *Appl. Phys. Lett.*, 2015, **106**, 012903.
- P. Fu, Z. Xu, R. Chu, W. Li, G. Zang and J. Hao, *Mater. Chem. Phys.*, 2010, **124**, 1065–1070.
- R. D. Shannon, *Acta Crystallogr., Sect. A: Cryst. Phys., Diffraction, Theor. Gen. Crystallogr.*, 1976, **32**, 751–767.
- B. Xu, Y. Ye and L. E. Cross, *J. Appl. Phys.*, 2000, **87**, 2507–2515.
- T. Tunkasiri and G. Rujijanagul, *J. Mater. Sci. Lett.*, 1996, **15**, 1767–1769.
- A. Kishimoto, K. Koumoto and H. Yanagida, *J. Mater. Sci.*, 1989, **24**, 698–702.
- Y. Yang, L. Y. Zhang, K. Zhu and Y. L. Liu, *J. Appl. Phys.*, 2011, **109**, 083517.
- K. C. V. Lima, A. G. S. Filho, A. P. Ayala, J. M. Filho, P. T. C. Freire, F. E. A. Melo, E. B. Araújo and J. A. Eiras, *Phys. Rev. B: Condens. Matter Mater. Phys.*, 2001, **63**, 184105.
- L. Mitoseriu, M. M. Carnasciali, P. Piaggio and P. Nanni, *J. Appl. Phys.*, 2004, **96**, 4378–4385.

- 30 R. Migoni, H. Bilz and D. Bäuerle, *Phys. Rev. Lett.*, 1976, **37**, 1155–1158.
- 31 R. Xu, B. Li, J. Tian, Z. Xu, Y. Feng, X. Wei, D. Huang and L. Yang, *Appl. Phys. Lett.*, 2017, **110**, 142904.
- 32 C. Luo, Q. Feng, N. Luo, C. Yuan, C. Zhou, Y. Wei, T. Fujita, J. Xu and G. Chen, *Chem. Eng. J.*, 2021, **420**, 129861.
- 33 Y. Huan, T. Wei, X. Wang, X. Liu, P. Zhao and X. Wang, *Chem. Eng. J.*, 2021, **425**, 129506.
- 34 J. Gao, Q. Liu, J. Dong, X. Wang, S. Zhang and J. F. Li, *ACS Appl. Mater. Interfaces*, 2020, **12**, 6097–6104.
- 35 X. Wang, Y. Huan, P. Zhao, X. Liu, T. Wei, Q. Zhang and X. Wang, *J. Materiomics*, 2021, **7**, 780–789.
- 36 Z.-G. Liu, M.-D. Li, Z.-H. Tang and X.-G. Tang, *Chem. Eng. J.*, 2021, **418**, 129379.
- 37 P. Peng, H. Nie, C. Zheng, G. Wang and X. Dong, *J. Am. Ceram. Soc.*, 2021, **104**, 2610–2620.